Quantum Transport and Band Structure Evolution under High Magnetic Field in Few-Layer Tellurene

Gang Qiu,[†,‡] Yixiu Wang,[§] Yifan Nie,[‖] Yongping Zheng,[‖] Kyeongjae Cho,[‖] Wenzhuo Wu,[‡,§] and Peide D. Ye[*,†,‡]

[†]School of Electrical and Computer Engineering, Purdue University, West Lafayette, Indiana 47907, United States
[‡]Birck Nanotechnology Center, Purdue University, West Lafayette, Indiana 47907, United States
[§]School of Industrial Engineering, Purdue University, West Lafayette, Indiana 47907, United States
[‖]Department of Materials Science and Engineering, The University of Texas at Dallas, Richardson, Texas 75080, United States

S *Supporting Information*

ABSTRACT: Quantum Hall effect (QHE) is a macroscopic manifestation of quantized states that only occurs in confined two-dimensional electron gas (2DEG) systems. Experimentally, QHE is hosted in high-mobility 2DEG with large external magnetic field at low temperature. Two-dimensional van der Waals materials, such as graphene and black phosphorus, are considered interesting material systems to study quantum transport because they could unveil unique host material properties due to the easy accessibility of monolayer or few-layer thin films at the 2D quantum limit. For the first time, we report direct observation of QHE in a novel low-dimensional material system, tellurene. High-quality 2D tellurene thin films were acquired from recently reported hydrothermal method with high hole mobility of nearly 3000 cm^2/(V s) at low temperatures, which allows the observation of well-developed Shubnikov−de Haas (SdH) oscillations and QHE. A four-fold degeneracy of Landau levels in SdH oscillations and QHE was revealed. Quantum oscillations were investigated under different gate biases, tilted magnetic fields, and various temperatures, and the results manifest the inherent information on the electronic structure of Te. Anomalies in both temperature-dependent oscillation amplitudes and transport characteristics were observed that are ascribed to the interplay between the Zeeman effect and spin−orbit coupling, as depicted by the density functional theory calculations.

KEYWORDS: Two-dimensional materials, tellurene, Shubnikov−de Haas oscillations, quantum Hall effect, Zeeman effect
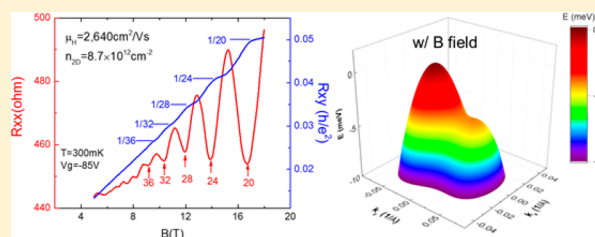
Two-dimensional electron gas (2DEG) is an important subject in condensed-matter physics for being a host to many exotic and conceptual physical phenomena. Quantum Hall effect (QHE), which refers to the effect of the transverse resistance being quantized into integer fractions of quantity h/e^2 in Hall measurement, is such a phenomenon that can only be observed in high-mobility 2DEGs. Traditionally, the confinement of electron motions within a 2D plane is realized by quantum wells formed in the inversion channel of silicon metal-oxide-semiconductor field-effect transistors (MOS-FETs)[1] or AlGaAs/GaAs heterojunctions.[2] In the past decade, the emergence of 2D materials has offered an alternative approach to achieving high-mobility 2DEGs in atomically thin layers. 2D materials are formed by an assembly of atomic layers bonded by weak van der Waals forces. The crystal structure of 2D materials yields a dangling-bond-free surface; consequently, the 2D material systems are less susceptible to mobility degradation than bulk materials, with thickness shrinking down to a few nanometers. QHE has been observed only in a few high-mobility 2D material systems such as graphene,[3−5] InSe,[6] and encapsulated few-layer phosphorene,[7−9] among thousands of predicted 2D materials.[10] Shubnikov−de Haas (SdH)

oscillations were observed in several other 2D materials such as WSe$_2$,[11,12] MoS$_2$,[13−15] ZrTe$_5$,[16−19] and Bi$_2$O$_2$Se.[20] For the first time, we report pronounced SdH oscillations and QHE in a novel 2D material: high-mobility air-stable few-layer Te films, coined as tellurene.

Tellurium (Te) is a group-VI narrow-bandgap p-type semiconductor with unique 1D van der Waals crystal structure. The atoms are covalently bonded into skew-symmetric helical chains, and the neighboring chains are bonded by van der Waals forces in the other two dimensions to form a trigonal crystal structure.[21−23] With proper crystal growth techniques, tellurium can also be arranged in a plane to form 2D morphology with bond-free surfaces (see Figure 1a). Bulk Te has a direct bandgap of ~0.35 eV[24] at the corner of Brillouin zone H (and H′) point, as shown in Figure 1b. The broken spatial inversion symmetry of the Te lattice structure gives rise to strong Rashba-like spin−orbit interaction;[24] therefore, a camelback-like electronic structure at the edge of the valence
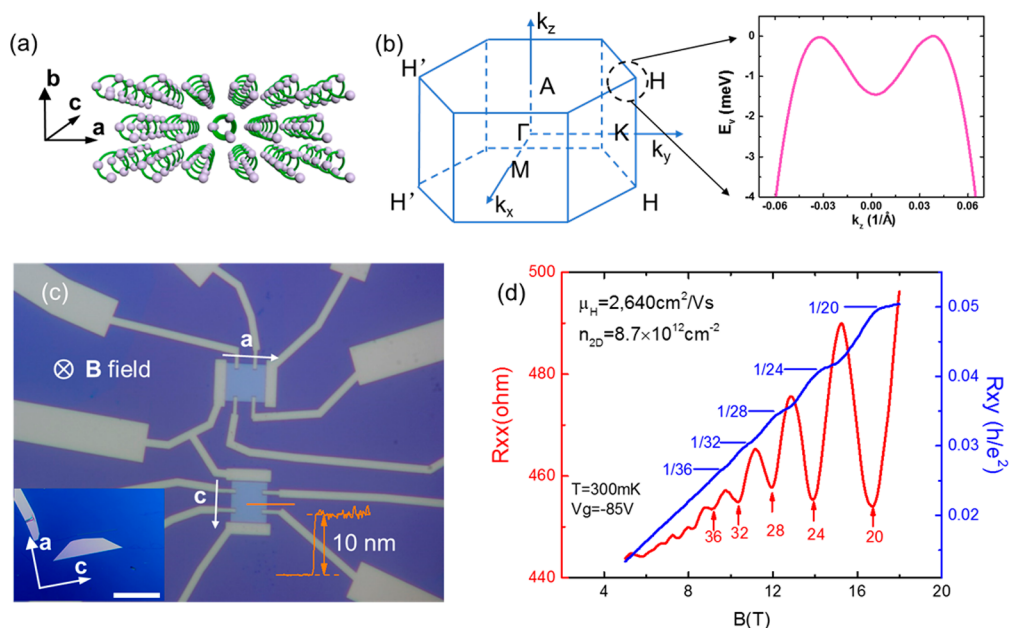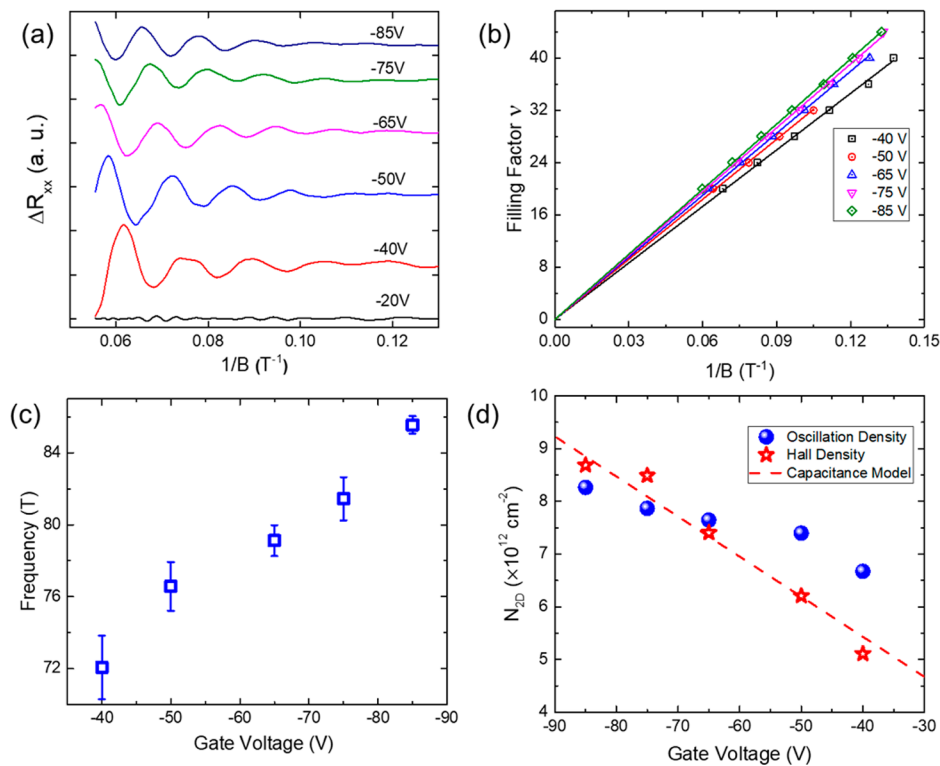
Figure 1. Shubnikov−de Haas oscillations and quantum Hall effect in 2D tellurene films. (a) Crystal structure of 1D van der Waals material tellurium. The collection of helical atom chains can be arranged into 2D films termed as tellurene. (b) Left: Brillouin zone of Te in momentum space. Right: Zoom-in features at H point of Brillouin zone where the valence band maxima reside. (c) Optical image of Hall-bar devices along two different crystal orientations fabricated from the same flake. Inset: As-grown flakes are usually in rectangular or trapezoidal shapes, where the 1D direction (*c* axis) is along the longer edge of the flake. The scale bar is 50 *μ*m. (d) QHE and SdH oscillations measured from a 10 nm thick flake.

band[22,25,26] was predicted by the density functional theory (DFT) calculations (right side of Figure 1b, the DFT computational details and complete band structure are presented in Supporting Notes 1 and 2). Weyl nodes were also theoretically predicted[24] and experimentally observed deeply embedded in the valence band of Te.[27] The earliest study on surface quantum states in bulk Te dates back to the early 1970s by von Klitzing et al.,[28−30] who later discovered QHE in silicon MOSFETs in 1980.[1] However, to our best knowledge, the evidence of QHE in Te is so far still missing, and even the reported quantum oscillations were so weak that they could only be seen in the second derivative d^2R_{xx}/dB^2.[28,29] Because Te has superior mobility compared with silicon, it is intriguing why quantum phenomena are so weak in Te. We postulate that this is due to the weak quantization of Te surface states in the wide triangular potential well. The characteristic width of the surface potential well λ is proportional to $\sqrt{\epsilon_s}$, where ϵ_s is the permittivity of the semiconductor. The large permittivity of tellurium (∼30) induces only a relatively small electrical field and wide potential well in tellurium surface. Therefore, the carriers are not tightly restrained near the surface to meet the rigid criteria of 2D confinement. In this work, we adopted a different strategy to impose stronger quantum confinement by employing 2D Te films. In general, the most widely used methods to acquire 2D thin films from van der Waals materials are mechanical exfoliation and chemical vapor deposition (CVD). Significant efforts have also been made to grow tellurium nanostructures; however, these methods yield either quasi-1D morphology[31−36] or small 2D flakes[37] that are unsuitable for studying magneto-transport. It is also very difficult to study transport properties of monolayer tellurene grown on conducting graphene surface by molecular beam epitaxy[38,39] because it requires monolayer transfer and process.[40−42] Recently, a liquid-based growth method[43] was proposed to

obtain large-scale 2D tellurene films with lateral sizes over 50 μm × 100 μm and thicknesses ranging from tens of nanometers down to few layers. These nanofilms were verified with high-crystal quality by crystallographic and spectroscopic techniques and offered a new route to explore the potential for electronic device applications[43] and magneto-transport studies.[44] To study quantum transport, flakes with thickness around 8−10 nm are desired because (1) high crystal quality is still preserved with hole mobility nearly 3000 cm^2/(V s) at liquid helium temperature and (2) the physical confinement in the out-of-plane direction is strong enough to impose sufficient 2D confinement.

The liquid-solution-based Te flake synthesis method was described in ref 42 (also see Supporting Note 3). As-grown tellurene flakes were dispensed onto heavily doped p-type silicon wafer with a 300 nm SiO$_2$ capping layer, which served as a universal back gate to modulate the Fermi level of Te samples. A standard six-terminal Hall-bar device was defined by electron beam lithography, and metallization was carried out by an electron beam evaporator. The hydrothermal growth method usually yields rectangular or trapezoidal flakes (see inset of Figure 1c) where the helical axis of the crystal is aligned with the long edge of the flakes, which facilitates our fabrication and measurement. This property was confirmed by detailed physical characterization such as transmission electron microscopy (TEM) and angle-resolved Raman spectroscopy.[43,44] To verify the anisotropic transport, we used a dry etching technique to trim the flakes into two identical rectangles but in different crystal orientations, one along the atomic chain direction (*c* axis) and the other one along the van der Waals force direction (*a* axis), and fabricated Hall bar structures accordingly (for device fabrication process and characterization, see Supporting Note 4). High work function metal palladium (Pd) was used to accommodate the hole transport. From four terminal measurements, we found that

Figure 2. Gate dependence of Shubnikov−de Haas oscillations versus $1/B$. (a) Oscillation amplitude under different gate biases. Oscillations were resolved only when the negative gate bias was large enough. The amplitudes were extracted by subtracting a smooth background from R_{xx}. (b) Landau fan diagram under different gate bias. Each data point represents the value of $1/B$, where the νth minimum of R_{xx} occurs. All of the lines have an intercept near zero, indicating the standard phase of oscillations. (c) Oscillation frequencies as a function of gate bias. The frequencies were extracted from the slope in panel b, and the error bars come from the linear fitting. (d) Comparison of 2D carrier density measured from oscillation frequencies (blue sphere) and Hall resistance (red pentagrams) and calculated from capacitance model (dotted line).

the Pd−Te interface formed good contacts even at low temperatures (see Supporting Note 5). The optical image of a typical pair of devices fabricated on a 10 nm thick flake is shown in Figure 1c. We determined that the helical chain direction exhibits ∼30% higher Hall mobility (for more discussion, see Supporting Notes 6 and 7). This ratio is close to the field-effect mobility anisotropic ratio measured at room temperature.[43] It was also noticed that the SdH oscillations and QHE features were more distinguishable along the *a* axis. Because the SdH oscillations are related to the in-plane cyclotron motions and QHE plateaus occur at metrological standard value of resistance irrelevant of device geometry, the data we presented in the latter part of the paper are acquired from devices along the *a* axis simply for its stronger oscillation signal and soundness of data interpretation.

Figure 1d shows the typical longitudinal resistance (R_{xx}) and transverse resistance (R_{xy}) of a 10 nm thick sample as a function of out-of-plane magnetic field measured at 300 mK with −85 V gate bias. From the slope of R_{xy} in the small B-field regime, the sheet carrier density of 8.7×10^{12} cm^{-2} (positive slope indicates hole is dominant carrier type) was extracted from the equation $n_{2D} = 1/eR_H$, where R_H is the Hall coefficient, with corresponding Hall mobility of 2640 cm^2/(V s) derived from $\mu_{Hall} = \frac{L}{W} \frac{1}{R_{xx} n_{2D} e}$. Well-developed SdH oscillations were observed in longitudinal resistance, and the onset occurs at ∼5 T, from which we can estimate the quantum mobility to be ∼2000 cm^2/(V s) from the criteria of SdH oscillation onset, $\omega_c \tau > 1$ (cyclotron frequency $\omega_c = eB/m^*$, τ is the relaxation time, and m^* is the hole effective mass in Te films), close to

the mobility value obtained from Hall measurement. At large B fields, the transverse resistance shows a series of quantum Hall plateaus at the values of integer fraction of resistance quanta h/e^2, although the plateaus are not completely flat due to the broadening effect. The filling factors were calculated by normalizing R_{xy} with metrological standard value of h/e^2. With the capacity of our equipment of 18 T magnetic field, the lowest filling factor ν we can observe is 20. An interval of 4 was found between the filling factors of neighboring plateaus, indicating a four-fold Landau level degeneracy. The four-fold degeneracy can be factored into two parts: (1) the spin degeneracy factor $g_s = 2$ and (2) the valley degeneracy factor $g_v = 2$ originating from H and H′ points in Brillouin zone, similar to the case in graphene (K and K′ points). Our tellurene samples show much better resolved SdH oscillations than previous works on surface states of bulk Te due to the high quality of 2D tellurene films and enhanced quantum confinement. We also found that QHE and SdH oscillations become weaker and eventually undetectable in thicker flakes (see Supporting Note 8).

We then applied different gate bias to tune the carrier density and studied the gate dependence of oscillation frequencies. The oscillation amplitudes were extracted by subtracting a smooth background from original data of R_{xx} and are plotted versus $1/B$ in Figure 2a. Strong oscillations with constant frequency $\Delta(1/B)$ are well developed with a negative gate bias over −40 V. However, at lower (absolute value of) gate bias, no pronounced oscillations can be observed because of the lower mobility at subthreshold regime, where the carrier concentration is low. This indicates that the impurity scattering
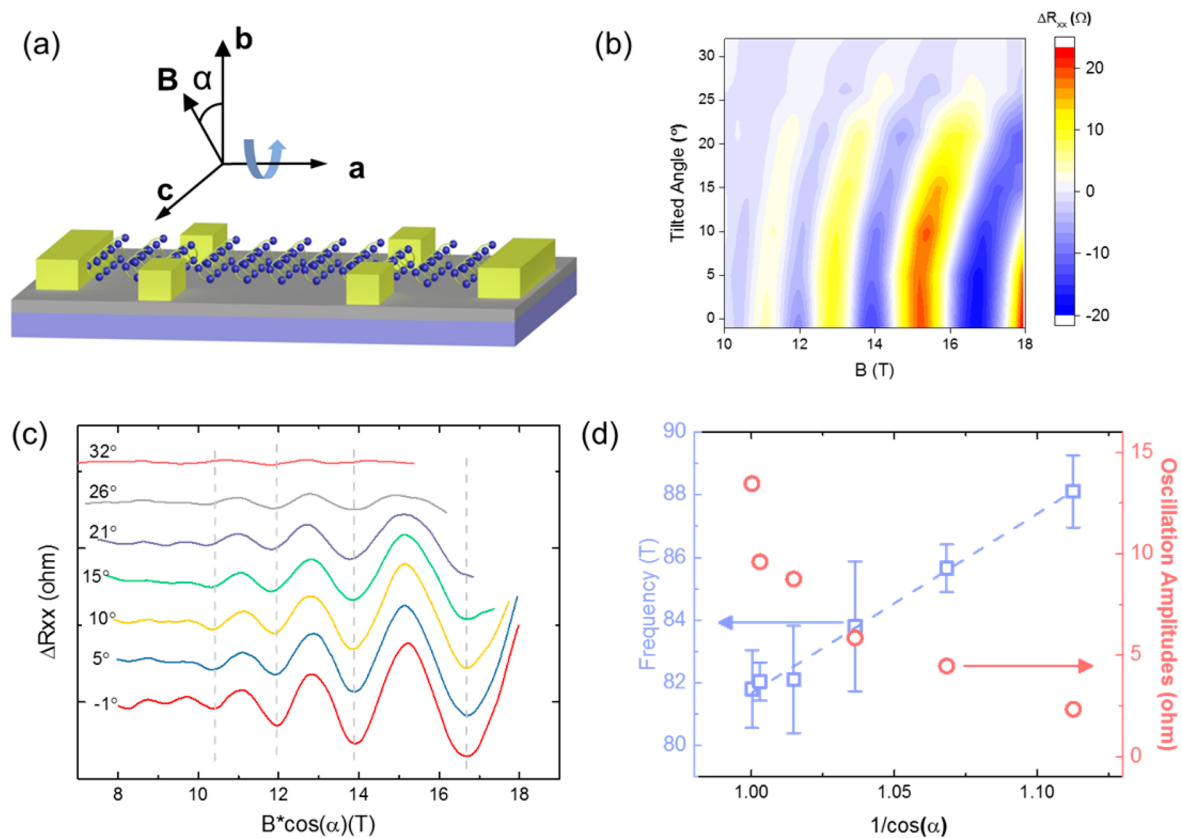
Figure 3. Angle dependence of oscillation frequencies. (a) Schematic configuration for angle-resolved oscillation frequency measurement. (b) Color map of oscillation amplitude as a function of B field and tilted angles. (c) Oscillation amplitudes plotted against perpendicular magnetic field component $B \times \cos(\alpha)$. (d) Oscillation frequencies (blue squares, left axis) and amplitudes (red circles, right axis) as a function of $1/\cos(\alpha)$. The error bars arise from the Lorentz peak fitting of FFT results. The dashed line shows a linear relationship between oscillation frequency and $1/\cos(\alpha)$, a signature of 2D Fermi surface.

is still dominant, like most of the 2D materials, and there is still large room to enhance transport properties through methods such as hexagonal boron nitride (h-BN) capping. Landau fan diagram was constructed by plotting the value of $1/B$, where the νth minimum of R_{xx} occurs against its corresponding filling factor as a common practice. Landau index n is related to the filling factor ν through the equation $\nu = g_s g_v(n)$, where g_s and g_v are spin and valley degeneracy of two, respectively. All of the data points fall onto a line that can be extrapolated toward zero intercept (fitting error within ± 0.2), indicating the standard phase of oscillations. The oscillation frequency B_F is derived from the slope of the Landau fan diagram in Figure 2b, from which 2D carrier density n_s can be estimated by substituting the frequency into the equation of frequency−density relationship, $n_s = g_s g_v e B_F / h$. We also compare the oscillation carrier density (blue spheres) and Hall density (red pentagrams) in Figure 2c. The orange dashed line is calculated from the gate capacitance model $n_{2D} = \frac{1}{e} C_g (V_g - V_{th})$. The Hall densities, oscillation densities, and densities calculated from capacitance model match quite well within a reasonable margin.

To better understand the two-dimensionality of Fermi surface in tellurene, we carried out angle-resolved SdH oscillation measurements in tilted magnetic fields. The experiment configuration is illustrated in Figure 3a. The sample was rotated along the a axis by angle α, and the corresponding 2D Fermi surface is associated with SdH oscillation frequency through the equation $B_F(\alpha) = h S_F(\alpha)/$ $4\pi^2 e$. The oscillation amplitudes with different angles are plotted in a color map in Figure 3b. A shift of oscillation features toward higher magnetic field was captured as the tilted angle increases. For clarity, the angle-resolved SdH oscillation amplitudes were plotted against perpendicular magnetic field component $B_\perp = B \times \cos(\alpha)$ in Figure 3c, where the minima of oscillations occur at the same value. The oscillations are too vague to be distinguished for $\alpha > 35°$, and in the $0 < \alpha < 32°$ regime, the oscillation features also diminish as we increase the angle (see Figure 3d, right axis). The physics origin of the fast damping of oscillation amplitudes in tilted magnetic fields is under further investigation. By performing fast Fourier transform, we found that the oscillation frequency $B_F(\alpha)$, or the projection of Fermi surface $S_F(\alpha)$, is linear dependent on the factor $1/\cos(\alpha)$, another signature of two dimensionality of carrier motions.

Finally, we studied the temperature dependence of SdH oscillations and the evidence of the band structure evolution with large magnetic field originated from the interplay of Zeeman splitting and spin−orbit coupling. Temperature-dependent SdH oscillation amplitudes were first investigated as a common practice to extract effective mass. As seen in Figure 4a, the period and the phase of the oscillations are independent of temperature, and the amplitudes exhibit a diminishing trend with rising temperature in general. For temperature higher than 5 K, the amplitudes decrease monotonically, as we expected, and can be fitted with the classical Lifshitz−Kosevich equation $\Delta R_{xx} \propto \frac{2\pi^2 k_B m^* T / \hbar e B}{\sinh(2\pi^2 k_B m^* T / \hbar e B)}$.
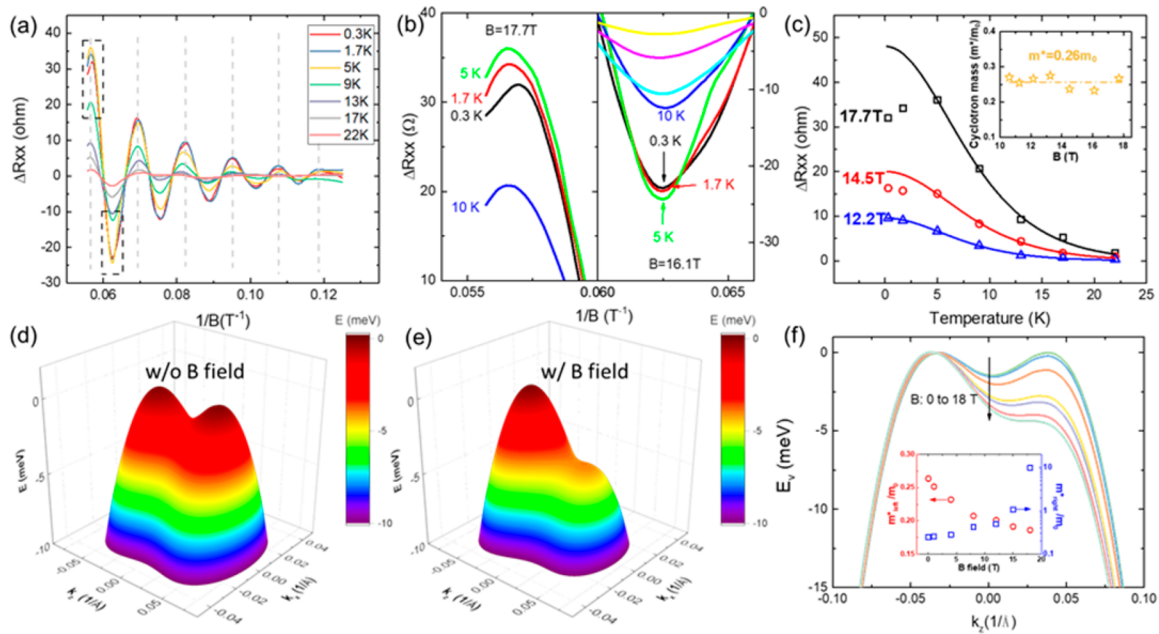
Figure 4. Anomalous temperature dependence of oscillation amplitudes. (a) Oscillation amplitudes measured at various temperatures. (b) Zoomed-in features of two oscillation peaks at 17.7 and 16.1 T as highlighted in dashed boxes in panel a. (c) Extracted oscillation peak amplitudes under different magnetic field as a function of temperature. The solid line is the fitting curve from Lifshitz−Kosevich equation with data points $T >$ 5 K. Under large magnetic field, the low-temperature data points deviated from fitting curves, which was also captured in panel b. Inset: The effective cyclotron mass was extracted to be $0.26m_0$. (d,e) Camelback shape of valence band maxima vicinity without and with external B field. (f) Cross-section of valence band edge cut along the k_z direction. Inset: The effective mass of light and heavy pocket holes under different magnetic fields.
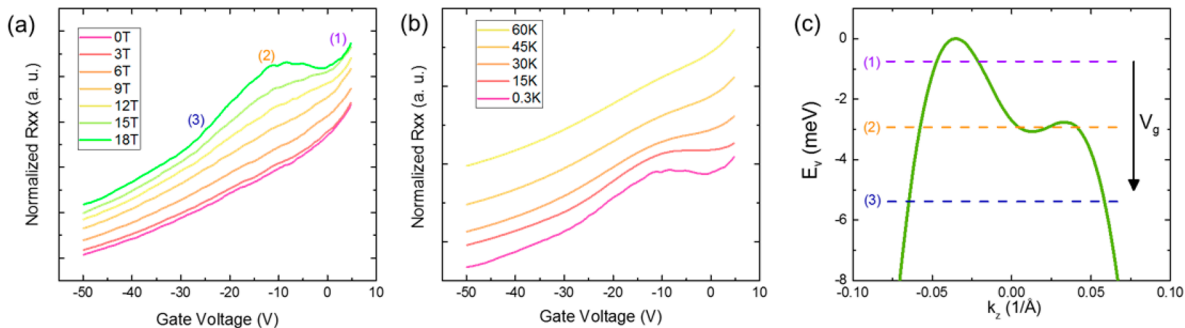
Figure 5. Anomalous increase in R_{xx} when sweeping gate voltage toward negative bias. The abnormal increase measured under different (a) magnetic field and (b) different temperature. (c) Explanation of the abnormal increase of resistance. As we sweep gate in the reverse direction, the Fermi energy will be pulled downward and slightly enter the valence band. (1), (2), and (3) represent three typical scenarios corresponding to the points with the same notations in panel a.

The fitted curves are plotted as solid lines in Figure 4c, and the effective mass m^* can be extracted to be ∼$0.26m_0$ (here m_0 is the free electron mass) correspondingly, which is very close to our DFT calculation. From the extracted effective mass and quantum mobility, we can estimate the Landau level broadening on the scale of $\Gamma = \frac{\hbar e}{\mu_q m^*} \approx 25$ K, which is much more dominant than temperature broadening of 300 mK, indicating that the limitation of experimental resolution comes from the disorders in the system. The carrier lifetime τ can also be extracted by combining the thermal factor as well as the Dingle factor $\Delta R_{xx} \propto R_T R_D$ where the Dingle factor R_D takes the form $R_D = \exp\left(-\frac{\pi m^*}{\tau e B}\right)$. By reshaping the first equation and taking the semiology plot, we shall get $\ln(\Delta R_{xx} \cdot B \cdot \sinh \lambda(T)) = -\frac{\pi m^*}{\tau e B} + const$. Therefore, a linear

trend is observed in $\ln(\Delta R_{xx} \cdot B \cdot \sinh \lambda(T))$ against $1/B$ plot (see Supporting Note 9 and Figure S8), where the carrier lifetime of 0.10 ps can be extracted from the slope. By carefully examining the amplitude at each oscillation peak (zoomed in features are plotted in Figure 4b), we found that at temperature <5 K the data points do not coincide with fitted curves, as shown in Figure 4b,c, and the discrepancy is more significant at larger B field. The deviation of oscillation amplitudes is abnormal, suggesting that the average effective mass is heavier under the conditions of large magnetic fields and low temperatures. This can be tentatively explained by the band structure reshaping with the existence of external magnetic field. An insightful picture of the band structure evolution is given by DFT calculations under magnetic field perpendicular to the helical axis, with spin−orbit coupling taken into consideration, as shown in Figure 4d,e (details of the DFT calculation are discussed in Supporting Note 2). The

broken spatial inversion symmetry of Te crystal introduces Rashba-like spin−orbit coupling (SOC), which causes a lateral shift of spin-up and spin-down subbands in different directions along the k_z axis in the band dispersion diagram and forms a camelback structure, as shown in Figure 4d. With the presence of external B field, the degenerate energy levels for spin-up and spin-down states will also be lifted by Zeeman splitting energy: $E_z = g\mu_B B$, where g is the g factor and μ_B is the Bohr magneton. The interplay of SOC and Zeeman splitting introduces band evolution, as shown in Figure 4e. If we take a cross-section of band dispersion along the camelback direction (k_z direction), then we can clearly see that the two degenerate valleys will be split into one heavy hole pocket and one light hole pocket with increasing magnetic field (Figure 4f). Note that the oscillation features were captured under large negative gate bias, which is equivalent to pulling the Fermi level slightly inside the valence band, as shown in the dashed line in Figure 5c. Under sufficiently low temperature condition, the Boltzmann distribution ensures that the states responsible for transport will be confined within a very narrow range (several kT) near the Fermi level, and the carriers in the right branch of Figure 4f will dominate the transport behavior, which exhibits larger effective mass. As the temperature rises, such effect will be mitigated by temperature broadening as the fine electrical structure becomes undetectable, and the carriers in both pockets will participate in transport, and hence the average effective mass will fall back to the classical value. The DFT calculation (see inset of Figure 4f) suggests that as we increase the external B field to 18 T, the calculated effective mass of the light hole pocket slightly drops from 0.26 to $0.19m_0$, whereas the effective mass in the heavy hole pocket increases drastically to $\sim9.8m_0$ (see inset of Figure 4f), which qualitatively matches our experiment results.

Another evidence related to this effect is the anomalous transfer characteristics of R_{xx} versus gate bias under large magnetic field. For normal 2DEG systems, in the linear regime, the channel resistance should drop inversely as we raise overdrive voltage $|V_g - V_{th}|$. Here V_{th} is the threshold voltage from which the channel is turned on. However, in tellurene films under large external magnetic fields and at low temperatures, as we sweep the gate voltage in the reverse direction, the resistance sees an abnormal rise around −5 V, which peaks at around −10 V, and drops again at around −20 V, as shown in the top curve in Figure 5a. We further verified that this anomalous increase in resistance has a strong dependence on the magnetic field (see Figure 5a). Therefore, we believe it is also related to the aforementioned Zeeman-effect-induced band structure evolution. We denote three representative situations (1), (2), and (3) as we lower the Fermi level in Figure 5c, corresponding to spots (1), (2), and (3) in the transfer curves in Figure 5a. At positions (1) and (3), the transport behavior can be explained by a classical semiconductor picture. At position (2), however, the carriers in the heavy pocket start to dominate the transport, and the resistance will increase because of the larger average effective mass. This anomalous resistance bump will also vanish at higher temperature (shown in Figure 5b) as the temperature broadens the Boltzmann distribution, making it difficult to distinguish such fine structures in the electronic band. In general, the camel-like electronic structure remains the same in 2D tellurene flakes with the thickness of 8−12 nm, similar to trigonal Te bulks.

In conclusion, we realized strong 2D confinement in a novel van der Waals 2D material tellurene by taking advantage of recently developed liquid-phase-grown high-mobility air-stable tellurene ultrathin films. QHE was observed on Te for the first time with four-fold degeneracy. Well-developed SdH oscillations were thoroughly investigated under different gate bias, temperatures, and tilted magnetic fields. Anomaly in cyclotron effective mass and transfer characteristics at large magnetic fields and low temperatures were also observed, which is attributed to the interplay of Zeeman splitting and strong Rashba-like spin−orbit coupling in Te. Our work revealed the intriguing electronic structure of Te through quantum transport and demonstrated the high quality of the novel 2D tellurene material system, which is even suitable to explore exotic topological phenomena[23,24,27,42] in Te.

■ ASSOCIATED CONTENT

ⓈSupporting Information

The Supporting Information is available free of charge on the ACS Publications website at DOI: 10.1021/acs.nano-lett.8b02368.

> DFT calculation methods, device fabrication and measurement details, discussion on contact resistance, anisotropic transport, and additional SdH oscillation data (PDF)

■ AUTHOR INFORMATION

Corresponding Author

*E-mail: yep@purdue.edu. Tel: (765)-494-7611.

ORCID Ⓞ

Yifan Nie: 0000-0003-4771-3633
Wenzhuo Wu: 0000-0003-0362-6650
Peide D. Ye: 0000-0001-8466-9745

Author Contributions

P.D.Y. conceived and supervised the project. P.D.Y. and G.Q. designed the experiments. Y.W. and W.W. synthesized the material. G.Q. fabricated the devices and performed the low-temperature magneto-transport measurement. P.D.Y. and G.Q. analyzed the data. Y.N., Y.Z., and K.C. performed DFT calculations. G.Q. and P.D.Y. wrote the manuscript. All authors have discussed the results and commented on the paper.

Notes

The authors declare no competing financial interest.

■ ACKNOWLEDGMENTS

■ REFERENCES

(1) Klitzing, K. V.; Dorda, G.; Pepper, M. New method for high-accuracy determination of the fine-structure constant based on quantized hall resistance. *Phys. Rev. Lett.* **1980**, *45*, 494−497.

(2) Tsui, D. C.; Gossard, A. C. Resistance standard using quantization of the Hall resistance of GaAs-Al$_x$Ga$_{1-x}$As heterostructures. *Appl. Phys. Lett.* **1981**, *38*, 550.

(3) Zhang, Y. B.; Tan, Y. W.; Stormer, H. L.; Kim, P. Experimental observation of the quantum Hall effect and Berry's phase in graphene. *Nature* **2005**, *438*, 201−204.

(4) Novoselov, K. S.; Jiang, Z.; Zhang, Y.; Morozov, S. V.; Stormer, H. L.; Zeitler, U.; Maan, J. C.; Boebinger, G. S.; Kim, P.; Geim, A. K. Room-Temperature Quantum Hall Effect in Graphene. *Science* **2007**, *315*, 1379−1379.

(5) Gusynin, V. P.; Sharapov, S. G. Unconventional integer quantum hall effect in graphene. *Phys. Rev. Lett.* **2005**, *95*, 146801.

(6) Bandurin, D. A.; Tyurnina, A. V.; Yu, G. L.; Mishchenko, A.; Zólyomi, V.; Morozov, S. V.; Kumar, R. K.; Gorbachev, R. V.; Kudrynskyi, Z. R.; Pezzini, S.; et al. High electron mobility, quantum Hall effect and anomalous optical response in atomically thin InSe. *Nat. Nanotechnol.* **2017**, *12*, 223−227.

(7) Li, L.; Yang, F.; Ye, G. J.; Zhang, Z.; Zhu, Z.; Lou, W.; Zhou, X.; Li, L.; Watanabe, K.; Taniguchi, T.; et al. Quantum Hall effect in black phosphorus two-dimensional electron system. *Nat. Nanotechnol.* **2016**, *11*, 593−597.

(8) Yang, J.; Tran, S.; Wu, J.; Che, S.; Stepanov, P.; Taniguchi, T.; Watanabe, K.; Baek, H.; Smirnov, D.; Chen, R.; Lau, C. N. Integer and Fractional Quantum Hall effect in Ultra-high Quality Few-layer Black Phosphorus Transistors. *Nano Lett.* **2018**, *18*, 229−234.

(9) Chen, X.; Wu, Y.; Wu, Z.; Han, Y.; Xu, S.; Wang, L.; Ye, W.; Han, T.; He, Y.; Cai, Y.; Wang, N. High-quality sandwiched black phosphorus heterostructure and its quantum oscillations. *Nat. Commun.* **2015**, *6*, 7315.

(10) Mounet, N.; Gibertini, M.; Schwaller, P.; Campi, D.; Merkys, A.; Marrazzo, A.; Sohier, T.; Castelli, I. E.; Cepellotti, A.; Pizzi, G.; Marzari, N. Two-dimensional materials from high-throughput computational exfoliation of experimentally known compounds. *Nat. Nanotechnol.* **2018**, *13*, 246−252.

(11) Fallahazad, B.; Movva, H. C. P.; Kim, K.; Larentis, S.; Taniguchi, T.; Watanabe, K.; Banerjee, S. K.; Tutuc, E. Shubnikov-de Haas Oscillations of High-Mobility Holes in Monolayer and Bilayer WSe$_2$: Landau Level Degeneracy, Effective Mass, and Negative Compressibility. *Phys. Rev. Lett.* **2016**, *116*, 086601.

(12) Movva, H. C.; Fallahazad, B.; Kim, K.; Larentis, S.; Taniguchi, T.; Watanabe, K.; Banerjee, S. K.; Tutuc, E. Density-Dependent Quantum Hall States and Zeeman Splitting in Monolayer and Bilayer WSe$_2$. *Phys. Rev. Lett.* **2017**, *118*, 247701.

(13) Cui, X.; Shih, E. M.; Jauregui, L. A.; Chae, S. H.; Kim, Y. D.; Li, B.; Seo, D.; Pistunova, K.; Yin, J.; Park, J. H.; et al. Low temperature Ohmic Contact to Monolayer MoS$_2$ by van der Waals Bonded Co/h-BN Electrodes. *Nano Lett.* **2017**, *17*, 4781−4786.

(14) Cui, X.; Lee, G. H.; Kim, Y. D.; Arefe, G.; Huang, P. Y.; Lee, C. H.; Chenet, D. A.; Zhang, X.; Wang, L.; Ye, F.; et al. Multi-terminal transport measurements of MoS$_2$ using a van der Waals heterostructure device platform. *Nat. Nanotechnol.* **2015**, *10*, 534−540.

(15) Wu, Z.; Xu, S.; Lu, H.; Khamoshi, A.; Liu, G. B.; Han, T.; Wu, Y.; Lin, J.; Long, G.; He, Y.; et al. Even-odd layer-dependent magnetotransport of high-mobility Q-valley electrons in transition metal disulfides. *Nat. Commun.* **2016**, *7*, 12955.

(16) Yu, W.; Jiang, Y.; Yang, J.; Dun, Z. L.; Zhou, H. D.; Jiang, Z.; Lu, P.; Pan, W. Quantum Oscillations at Integer and Fractional Landau Level Indices in Single-Crystalline ZrTe$_5$. *Sci. Rep.* **2016**, *6*, 35357.

(17) Qiu, G.; Du, Y.; Charnas, A.; Zhou, H.; Jin, S.; Luo, Z.; Zemlyanov, D. Y.; Xu, X.; Cheng, G. J.; Ye, P. D. Observation of Optical and Electrical In-Plane Anisotropy in High-Mobility Few-Layer ZrTe$_5$. *Nano Lett.* **2016**, *16*, 7364−7369.

(18) Liu, Y.; Yuan, X.; Zhang, C.; Jin, Z.; Narayan, A.; Luo, C.; Chen, Z.; Yang, L.; Zou, J.; Wu, X.; et al. Zeeman splitting and dynamical mass generation in Dirac semimetal ZrTe$_5$. *Nat. Commun.* **2016**, *7*, 12516.

(19) Zheng, G.; Lu, J.; Zhu, X.; Ning, W.; Han, Y.; Zhang, H.; Zhang, J.; Xi, C.; Yang, J.; Du, H.; et al. Transport evidence for the three-dimensional Dirac semimetal phase in ZrTe$_5$. *Phys. Rev. B: Condens. Matter Mater. Phys.* **2016**, *93*, 115414.

(20) Wu, J.; Yuan, H.; Meng, M.; Chen, C.; Sun, Y.; Chen, Z.; Dang, W.; Tan, C.; Liu, Y.; Yin, J.; et al. High electron mobility and quantum oscillations in non-encapsulated ultrathin seconducting Bi$_2$O$_2$Se. *Nat. Nanotechnol.* **2017**, *12*, 530−534.

(21) Skadron, P.; Johnson, V. A. Anisotropy and annealing behavior in extrinsic single-crystal tellurium. *J. Appl. Phys.* **1966**, *37*, 1912−1917.

(22) Peng, H.; Kioussis, N.; Snyder, G. J. Elemental tellurium as a chiral p-type thermoelectric material. *Phys. Rev. B: Condens. Matter Mater. Phys.* **2014**, *89*, 195206.

(23) Agapito, L. A.; Kioussis, N.; Goddard, W. A.; Ong, N. P. Novel family of chiral-based topological insulators: Elemental tellurium under strain. *Phys. Rev. Lett.* **2013**, *110*, 176401.

(24) Hirayama, M.; Okugawa, R.; Ishibashi, S.; Murakami, S.; Miyake, T. Weyl Node and Spin Texture in Trigonal Tellurium and Selenium. *Phys. Rev. Lett.* **2015**, *114*, 206401.

(25) Furukawa, T.; Shimokawa, Y.; Kobayashi, K.; Itou, T. Observation of current-induced bulk magnetization in elemental tellurium. *Nat. Commun.* **2017**, *8*, 1−5.

(26) Anzin, V. B.; Kosichkin, Y. V.; Veselago, V. G.; Bresler, M. S.; Farbstein, I. I.; Itskevich, E. S.; Sukhoparov, V. A. Inversion asymmetry splitting of Landau levels in tellurium. *Solid State Commun.* **1970**, *8*, 1773−1777.

(27) Nakayama, K.; Kuno, M.; Yamauchi, K.; Souma, S.; Sugawara, K.; Oguchi, T.; Sato, T.; Takahashi, T. Band splitting and Weyl nodes in trigonal tellurium studied by angle-resolved photoemission spectroscopy and density functional theory. *Phys. Rev. B: Condens. Matter Mater. Phys.* **2017**, *95*, 125204.

(28) von Klitzing, K.; Landwehr, G. Surface Quantum States in Tellurium. *Solid State Commun.* **1971**, *9*, 2201−2205.

(29) Silbermann, R.; Landwehr, G. Surface Quantum Oscillations in Accumulation and Inversion Layers on Tellurium. *Solid State Commun.* **1975**, *16*, 1055−1058.

(30) von Klitzing, K. Magnetophonon Oscillatinos in Tellurium under Hot Carrier Conditions. *Solid State Commun.* **1974**, *15*, 1721−1725.

(31) Hawley, C. J.; Beatty, B. R.; Chen, G.; Spanier, J. E. Shape-controlled vapor-transport growth of tellurium nanowires. *Cryst. Growth Des.* **2012**, *12*, 2789−2793.

(32) Wang, Q.; Li, G. D.; Liu, Y. L.; Xu, S.; Wang, K. J.; Chen, J. S. Fabrication and growth mechanism of selenium and tellurium nanobelts through a vacuum vapor deposition route. *J. Phys. Chem. C* **2007**, *111*, 12926−12932.

(33) Sen, S.; Bhatta, U. M.; Kumar, V.; Muthe, K. P.; Bhattacharya, S.; Gupta, S. K.; Yakhmi, J. V. Synthesis of tellurium nanostructures by physical vapor deposition and their growth mechanism. *Cryst. Growth Des.* **2008**, *8*, 238−242.

(34) Geng, B.; Lin, Y.; Peng, X.; Meng, G.; Zhang, L. Large-scale synthesis of single-crystalline Te nanobelts by a low-temperature chemical vapour deposition route. *Nanotechnology* **2003**, *14*, 983−986.

(35) Mayers, B.; Xia, Y. One-dimensional nanostructures of trigonal tellurium with various morphologies can be synthesized using a solution-phase approach. *J. Mater. Chem.* **2002**, *12*, 1875−1881.

(36) Churchill, H. O.; Salamo, G. J.; Yu, S. Q.; Hironaka, T.; Hu, X.; Stacy, J.; Shih, I. Toward Single Atom Chains with Exfoliated Tellurium. *Nanoscale Res. Lett.* **2017**, *12*, 1−6.

(37) Wang, Q.; Safdar, M.; Xu, K.; Mirza, M.; Wang, Z.; He, J. Van der Waals epitaxy and photoresponse of hexagonal tellurium nanoplates on flexible mica sheets. *ACS Nano* **2014**, *8*, 7497−7505.

(38) Huang, X.; Guan, J.; Lin, Z.; Liu, B.; Xing, S.; Wang, W.; Guo, J. Epitaxial Growth and Band Structure of Te Film on Graphene. *Nano Lett.* **2017**, *17*, 4619−4623.

(39) Chen, J.; Dai, Y.; Ma, Y.; Dai, X.; Ho, W.; Xie, M. Ultrathin β-tellurium layers grown on highly oriented pyrolytic graphite by molecular-beam epitaxy. *Nanoscale* **2017**, *9*, 15945−15948.

(40) Zhu, Z.; Cai, X.; Yi, S.; Chen, J.; Dai, Y.; Niu, C.; Guo, Z.; Xie, M.; Liu, F.; Cho, J. H.; et al. Multivalency-Driven Formation of Te-Based Monolayer Materials: A Combined First-Principles and Experimental study. *Phys. Rev. Lett.* **2017**, *119*, 1−5.

(41) Xian, L. D.; Perez Paz, A.; Bianco, E.; Ajayan, P. M.; Rubio, A. Square selenene and tellurene: novel group IV elemental 2D materials with nontrivial topological properties. *2D Mater.* **2017**, *4*, 041003.

(42) Qiao, J.; Pan, Y.; Yang, F.; Wang, C.; Chai, Y.; Ji, W. Strong inter-chain coupling and exceptionally high carrier mobility in stretchable Te few-layers. *Science Bulletin* **2018**, *63*, 159−168.

(43) Wang, Y.; Qiu, G.; Wang, R.; Huang, S.; Wang, Q.; Liu, Y.; Du, Y.; Goddard, W. A.; Kim, M. J.; Xu, X.; et al. Field-effect transistors made from solution-grown two-dimensional tellurene. *Nat. Electron.* **2018**, *1*, 228−236.

(44) Du, Y.; Qiu, G.; Wang, Y.; Si, M.; Xu, X.; Wu, W.; Ye, P. D. One-Dimensional van der Waals Material Tellurium: Raman Spectroscopy under Strain and Magneto-Transport. *Nano Lett.* **2017**, *17*, 3965−3973.